Neurobiology of Stress 20 (2022) 100476

Contents lists available at ScienceDirect

Neurobiology of Stress

journal homepage: www.elsevier.com/locate/ynstr

Labelfree mapping and profiling of altered lipid homeostasis in the rat hippocampus after traumatic stress: Role of oxidative homeostasis

D. Parker Kelley [a], Ardalan Chaichi [b], Alexander Duplooy [a], Dhirendra Singh [a], Manas Ranjan Gartia [b,*], Joseph Francis [a,**]

[a] Comparative Biomedical Sciences, Louisiana State University School of Veterinary Medicine, Baton Rouge, LA, 70803, USA
[b] Department of Mechanical and Industrial Engineering, Louisiana State University, Baton Rouge, LA, 70803, USA

ARTICLE INFO

Keywords:
Stress
PTSD
Lipids
Raman
ROS
Cholesterol

ABSTRACT

Oxidative and lipid homeostasis are altered by stress and trauma and post-traumatic stress disorder (PTSD) is associated with alterations to lipid species in plasma. Stress-induced alterations to lipid oxidative and homeostasis may exacerbate PTSD pathology, but few preclinical investigations of stress-induced lipidomic changes in the brain exist. Currently available techniques for the quantification of lipid species in biological samples require tissue extraction and are limited in their ability to retrieve spatial information. Raman imaging can overcome this limitation through the quantification of lipid species *in situ* in minimally processed tissue slices. Here, we utilized a predator exposure and psychosocial stress (PE/PSS) model of traumatic stress to standardize Raman imaging of lipid species in the hippocampus using LC-MS based lipidomics and these data were confirmed with qRT-PCR measures of mRNA expression of relevant enzymes and transporters. Electron Paramagnetic Resonance Spectroscopy (EPR) was used to measure free radical production and an MDA assay to measure oxidized polyunsaturated fatty acids. We observed that PE/PSS is associated with increased cholesterol, altered lipid concentrations, increased free radical production and reduced oxidized polyunsaturated fats (PUFAs) in the hippocampus (HPC), indicating shifts in lipid and oxidative homeostasis in the HPC after traumatic stress.

1. Introduction

The brain is roughly 50% lipids by dry mass (Morell and Toews, 1996). Maintaining lipid and cholesterol (CHOL) homeostasis in the brain is critical for the maintenance of cell membranes, ion homeostasis, and cell signaling. Stress has long been known to increase serum cholesterol levels (Wertlake et al., 1958). CHOL concentrations in neuronal membranes control growth factor signaling (Kumar and Chattopadhyay, 2020) through allosteric alterations to TrkB receptors (BDNFR), modulating GPCR signaling (Prasanna et al., 2016, 2020), and may modulate the action of antidepressants (AD) (Kumar and Chattopadhyay, 2020; Prasanna et al., 2016, 2020). Furthermore, CHOL is a precursor to neuronally produced neurosteroids, which modulate GABAergic neurotransmission (Reddy, 2010) and Astrocyte derived (Shan et al., 2021) CHOL contributes both directly (Barres and Smith, 2001) and indirectly (Fester et al., 2009) to synaptogenesis (Goritz et al., 2005). CHOL is also a significant constituent of synaptic vesicles and plays a role in organizing lipid rafts (Korade and Kenworthy, 2008) at pre and post-synaptic densities, making CHOL and lipid pathways essential modulators of all neurotransmission, and therefore hippocampal (HPC) function (Payandeh and Volgraf, 2021). Other lipids likewise modulate synaptic function and are modulated by stress. Phosphatidylcholine (PC) concentrations modulate acetylcholine synthesis (Chung et al., 1995) and increase DAG generation in the context of oxidative stress in synaptosomes and (Mateos et al., 2008) ether PC species are reduced in the HPC by chronic unpredictable mild stress (Oliveira et al., 2016). Myelin sheaths are produced by oligodendrocytes and constitute 80% of brain cholesterol. Stress and glucocorticoids are now known to increase oligodendrogenesis and myelin formation in the HPC, a region that is not typically myelinated (Chetty et al., 2014) and increased myelin was also recently observed in the brains of PTSD, but not mTBI participants (Jak et al., 2020; Chao et al., 2015).

Post-Traumatic Stress Disorder (PTSD), Mild Traumatic Brain Injury (mTBI), and depression are also associated with alterations to lipid

* Corresponding author.
** Corresponding author.
E-mail addresses: mgartia@lsu.edu (M.R. Gartia), jfrancis@lsu.edu (J. Francis).

https://doi.org/10.1016/j.ynstr.2022.100476
Received 18 April 2022; Received in revised form 27 July 2022; Accepted 27 July 2022
Available online 11 August 2022
2352-2895/© 2022 Published by Elsevier Inc. This is an open access article under the CC BY-NC-ND license (http://creativecommons.org/licenses/by-nc-nd/4.0/).

species in plasma (Huguenard et al., 2020; Demirkan et al., 2013). One study using Raman imaging indicates that animal models of TBI are associated with alterations to lipid concentrations in the brain over time, particularly elevated CHOL (Surmacki et al., 2017). Elevated reactive oxygen species (ROS) production can lead to oxidative stress, a characteristic feature of a numerous diseases associated with elevated allostatic load including TBI (Cornelius et al., 2013), major depressive disorder (MDD) (Lindqvist et al., 2017), metabolic syndrome (Furukawa et al., 2004), diabetes (Leslie and Vartak, 2020), hypertension (Guidi et al., 2020), Lupus (Nuttall et al., 2003), and PTSD (Miller et al., 2018), among other associated conditions. Each of these conditions is also associated with alterations in peripheral lipid homeostasis, particularly increased LDL CHOL and Triglycerides (TG) and reductions of many phospholipid species, like phosphatidylcholine (PC) (Demirkan et al., 2013; Hu et al., 2017). Chronic or traumatic stress may therefore disturb broad organismic molecular and lipid homeostasis and whole organism allostasis (Barrett et al., 2016). Many of these effects have been studied in animal models, but very few investigations have focused on stress-induced alterations to lipid species in the brain of models of traumatic stress (Oliveira et al., 2016; Prasad et al., 2019).

LC-MS is the gold standard technique for quantitative measurements of lipid species in biological tissue (Cajka and Fiehn, 2014). However, classical lipidome analysis results in the loss of spatial information due to the requirements of tissue homogenization and lipid extraction, an important limitation of this technique (Prasad et al., 2019). Lipid concentrations modulate synaptic function, and spatial localization may be critical for the identification of brain circuit-specific alterations to lipid species. The ability to derive spatial information on lipid concentrations in the brain in animal models would surpass currently available methods and may improve our ability to understand and treat psychiatric diseases associated with stress (Prasad et al., 2019). Raman spectroscopy to study lipids has attracted particular attention in the field because of the strong Raman scattering of lipids provided by long nonpolar acyl chains in their structure (Czamara et al., 2015). Lipids have Raman bands in both the fingerprint (400–1800 cm^{-1}) and higher wavenumber group frequency regions (2800–3800 cm^{-1}) (Santos et al., 2016). The most typical characteristics of lipids originate from their hydrocarbon chains, which manifest themselves in 1200-1050 cm^{-1} (C–C stretch), 1250-1300 cm^{-1} (CH_3 scissor and twist), and 1400-1500 cm^{-1} (CH_2 scissor and twist) ranges (Movasaghi et al., 2007). At higher wavenumbers, strong Raman bands appear in the 2800-3100 cm^{-1} region assigned to C–H stretching of lipids (Czamara et al., 2015).

Based on these factors, we previously utilized Raman to investigate lipid alterations in a predator exposure and psychosocial stress model (PE/PSS) of PTSD and confirmed these results with MALDI imaging. We found that PE/PSS is associated with broad alterations to lipid homeostasis in the paraventricular thalamus (PVT), notably increased CHOL and Cholesterol Esters (ChE) and modifications to several phospholipid species (Chaichi et al., 2021).

In this study, we hypothesized that the PE/PSS model would be associated with increased CHOL and ChE concentrations and reduced PC, and distinct lipid profiles measured by principle components analysis (PCA) in the HPC (Fig. 1a). First, we confirmed the PE/PSS phenotype by measuring a previously published endpoint in this model

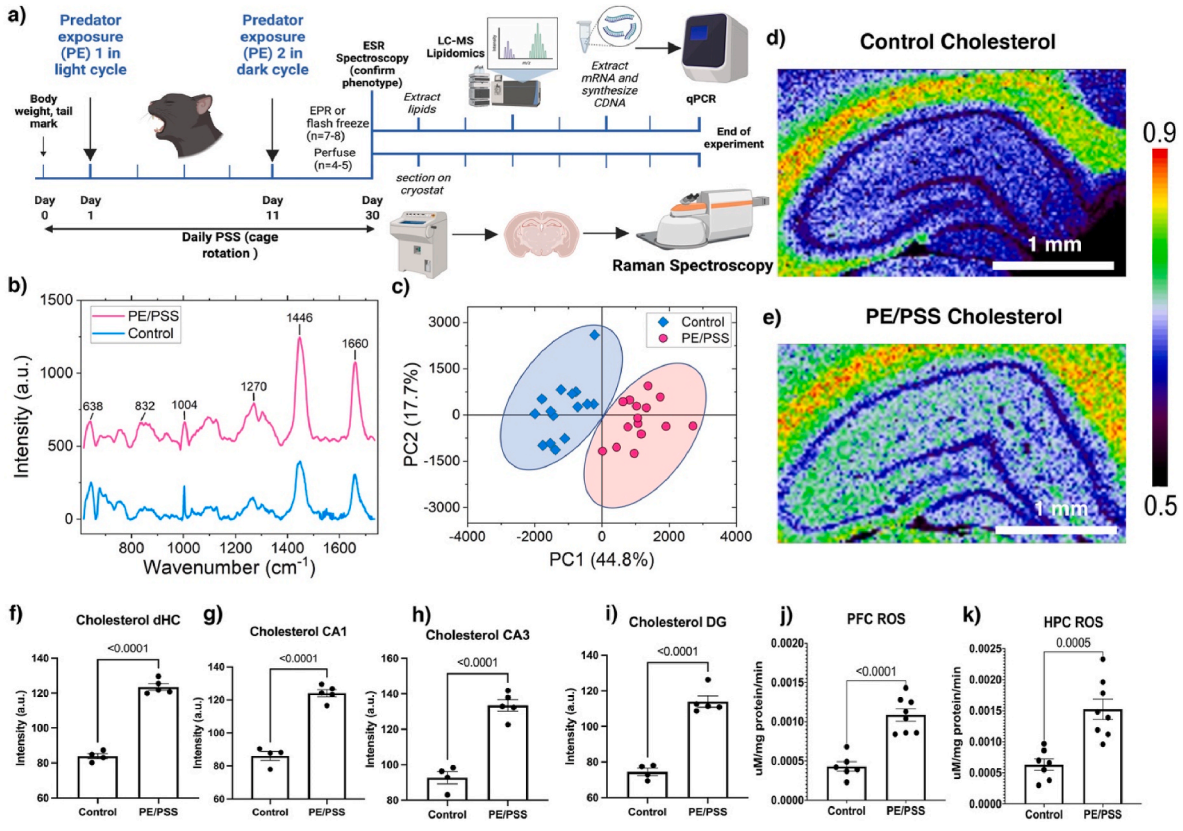

Fig. 1. a) Timeline of experimental procedure. Animals were sacrificed on day 31 and split into two groups. Group 1 prefrontal cortex (PFC) and hippocampus (HPC) tissue were removed and either immediately measured for ROS (EPR) or flash frozen for lipidomic or PCR analysis. Group 2 was transcardially perfused with paraformaldehyde (PFA) and whole brains were flash frozen, sectioned on a cryostat, and Raman was performed at a later date. b) Raman spectra between control and PE/PSS. c) PCA analysis of Raman spectra d) Raman heatmap of cholesterol for control e) Raman heatmap of cholesterol for PE/PSS. The colorbar represents the correlation coefficient. f) Quantification of Raman heatmap for cholesterol between control and PE/PSS for the dHC. g) Quantification of Raman heatmap for cholesterol for CA1. h) Quantification of the Raman heatmap for cholesterol for CA3. i) Quantification of the Raman heatmap for cholesterol for the dentate gyrus (DG). j) EPR spectroscopy data for the PFC exhibits increased ROS production in PE/PSS ($p < .0001$). k) EPR exhibits increased ROS production in the HPC ($p = .0005$).

(Wilson et al., 2013), ROS production in the prefrontal cortex (PFC) and HPC, which was upregulated after PE/PSS. Next, we implemented a dual forward/reverse approach to validate our technique by making a hypothesis, followed by testing it with Raman imaging, and then validating those results with data using an LC-MS-based lipidomic analysis and vice versa. We first utilized Raman to image and quantify CHOL and ChE concentrations in formalin-fixed coronal sections of the dorsal hippocampus (dHPC). We subsequently performed LC-MS-based lipidomics and confirmed elevations of three ChE species, in addition to acquiring data on hundreds of lipid species. We next performed PCA of the Raman and LC-MS data sets. We identified top targets from the LC-MS data through a bioinformatics analysis and quantified alterations to both individual lipid species and lipid classes. We then reversed the direction of our validation procedure by generating three hypotheses from top biomarkers that emerged from lipidomics and testing them with Raman. We hypothesized that phosphatidylcholine (PC) and phosphatidylserine (PS) would be downregulated, and triglyceride (TG) would be upregulated. We were able to reject the null hypothesis for all three species. For further validation, we chose two "control" lipids that were not identified as top targets in the lipidomic analysis, one target that was differentially expressed in the LC-MS data, cardiolipin (CL), and one that was not, phosphatidylinositol (PI). Neither target exhibited similar alterations between Raman and LC-MS. We subsequently measured mRNA expression of the major functional components of brain lipid homeostasis by qRT-PCR. We hypothesized that we would observe increased ApoE, Srebf2, and Cyp27a1 expression and reduced Srebf1. We rejected the null hypothesis for ApoE, Cyp27a1, and Srebf1, but not Srebf2.

To provide further insight into the implications of elevated ROS in this model, we quantified malondialdehyde (MDA) concentrations in the HPC. We observed decreased MDA in PE/PSS, which significantly correlated to reduced total lipid species (other than CHOL, ChE, and TG) measured by LC-MS. Furthermore, Raman analysis exhibited an increased intensity of peak at 1660 cm^{-1}, in PE/PSS animals, which indicates increased docosahexaenoic acid (DHA), a lipid species that exhibits protective effects against oxidative stress. Together, these data suggest a remodeling of lipid and oxidative molecular homeostasis in the HPC after PE/PSS. To our knowledge, this is the first time that Raman spectroscopy was used to measure lipid and CHOL species in the HPC of an animal model of traumatic stress and confirmed those data with a quantitative gold standard technique, LC-MS.

2. Results

2.1. Raman: PE/PSS altered the lipid profile of the dHPC

Fig. 1b shows the comparison of representative Raman spectra of PE/PSS and control brain tissue. The Raman features associated with lipids (1270, 1446, 1660 cm^{-1}) were intensified in the PE/PSS samples compared to the control. The intensity of the peak associated with phenylalanine (1004 cm^{-1}) did not change for PE/PSS and control. The peak at 1660 cm^{-1} is attributed to ω-3 fatty acid (docosahexanoic acid) in the brain (arising from sterol C═C stretching vibration). (Schultz and Levin, 2011).

The Raman band at 1446 cm^{-1} originates from the acyl group (CH_2 or CH_3 scissoring vibration). The peak at 1270 cm^{-1} is due to = CH in-plane deformation arising from unsaturated acid chains mainly in PC and PE of the brain (Schultz and Levin, 2011). The Raman band at 832 cm^{-1} (responsible for Proline) intensified in PE/PSS compared to the control. Fig. 1c shows the score plot using the first two principal components (PC1 and PC2) based on 15 representative Raman spectra from each group (PE/PSS (pink) and control (blue)). The score plot clustered these two groups distinctly with positive PC1 values for PE/PSS and negative PC1 for Raman spectra obtained from the control groups. Fig. 1d and e shows the cholesterol distribution in the HPC of control and PE/PSS samples, respectively. The Raman maps (blue = low; red = high) clearly show increased cholesterol in PE/PSS sample compared to the control. The corresponding weighted mean values for CHOL were calculated from the Raman maps of the dHPC (Fig. 1h) and subregions of the dHPC. Fig. 1i (CA1), Fig. 1j (CA3), and Fig. 1k (DG) indicate a widespread increase in CHOL that is independent of HPC circuit. Tracings of HPC subregions used for dHPC and subregion-specific quantification of CHOL are provided in Supplementary Figs. 1i and j.

2.2. PE/PSS is associated with increased ROS production in the PFC and HPC

We previously published that ROS production is increased in the PFC and HPC of this PE/PSS model (Wilson et al., 2013), which has emerged as a characteristic biomarker in this model system. We once again measured elevated ROS production in this study, confirming the phenotype. An unpaired two-tailed *t*-test revealed that compared to control, PE/PSS animals exhibited increased ROS production in the PFC ($n = 6–8$/group, $t = 6.200$, $df = 12$, $p < .0001$) and HPC ($n = 7–8$/group, $t = 4.559$, $df = 13$, $p = .0005$). (Fig. 1f and g).

2.3. Lipidomics: PE/PSS altered the lipid profile of the HPC measured by LC-MS

We extracted lipids from whole HPC tissue from control and PE/PSS animals and performed LC-MS-based lipidomics on the lipid extracts. In total, 774 individual lipid species were detected from 32 total classes of lipids. Phospholipids constituted a total of 72.75% of total measured lipids, with PC species alone accounting for 49.15%. All data analysis was performed on mass spectrum intensity data normalized by the mass of the sample (Supplementary Table 1).

Data was analyzed in two ways. 1) Bioinformatics analysis to identify the top 15 individual lipid species biomarkers between control and PE/PSS. This analysis was performed on all 774 individual lipid species. 2) Analysis of all 33 lipid classes: each lipid species was grouped and considered as part of its lipid class. The bioinformatics analysis exhibited 15 top individual lipid species between PE/PSS and control. This included 7 downregulated PC species (PC424pH, PC428H, PC4410H, PC405eH, PC363H, PC182p/242H, and PC60/180H), 3 upregulated TG species (TG181/182/182N, TG160/171/204N, TG160/160/226N), 1 downregulated PS species (PS414–H), 1 downregulated PG species (PG225/226-H), 1 downregulated PE species (PE180p/160H), and 2 downregulated dMePE species (dMePE344p-H, dMePE160/160-H). (Fig. 2a–c).

2.4. Bioinformatics analysis

Fig. 2a represents the partial least squares-discriminant analysis (PLS-DA) results for PE/PSS and control. PLS-DA revealed two distinct clusters with significantly differentially expressed metabolites shown on the Variable Importance for Projection (VIP) plot (Fig. 2b). This indicates that these two group of samples exhibit distinct expression patterns of the measured metabolites. The obtained PLS-DA model was validated by seven-fold Cross-Validation predictive residual (CV-ANOVA) and response permutation with 900 random re-classifications (random assignment of class labels to PE/PSS and control in order to test whether differences found between groups are significant). In the current experiment, the PLS-DA model covers 99.1% (R2Y) of total Y variation and 72.6% (R2X) of total X variation, and predictive ability Q2 is 72.6%. The permutation test revealed the model overfits due to the low amount of replicates vs. a large number of detected metabolites. "Overfit" means that the predictability is not excellent, but that will not substantially impact the presented results. The VIP plot in Fig. 2b shows the important lipid species identified by PLS-DA in descending order of importance. The graph represents the relative contribution of lipid species to the variance between the PE/PSS and control samples. Sample A is PE/PSS, and sample B is the control. A high VIP score indicates a greater contribution of the lipid species to the group separation. The red

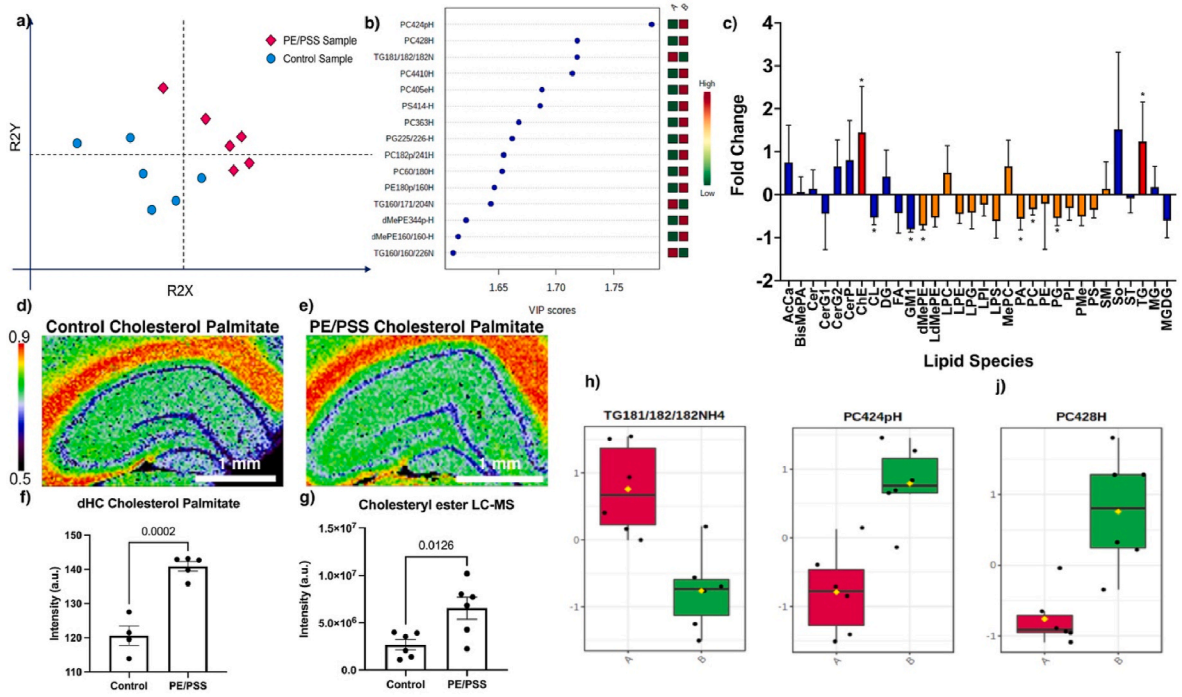

Fig. 2. a) Primary components analysis of control vs PE/PSS LC-MS lipidomic data. b) Bioinformatics analysis data of top 15 lipid species contributing to the PE/PSS phenotype compared to control. A indicates PE/PSS and B the control group. Red indicates upregulation and green indicates downregulation. c) Fold changes of difference in lipid expression in PE/PSS vs control. Orange indicates phospholipids. Red indicates triglyceride (TG) and cholesterol esters (ChE). Blue labels other lipids. d) Raman heatmap for cholesterol palmitate, a ChE, for the control group. e) Raman heatmap for cholesterol palmitate for the PE/PSS group. The colorbar represents the correlation coefficient. Scalebar = 1 mm. f) Quantification of Raman heatmap for cholesterol palmitate. g) LC-MS data for ChE species h-j) Box and whisker plots for TG181/182/182NH4, PC424pH, and PC428H. Red is the PE/PSS group. Green is the control group. (For interpretation of the references to color in this figure legend, the reader is referred to the Web version of this article.)

and green boxes on the right indicate whether the lipid concentration is increased (red) or decreased (green) in the tissue of the PE/PSS vs. control samples. The discriminating metabolites toward the clustering in the PLS-DA model were tested by regression coefficient plot with 95% jack-knifed confidence intervals where metabolites with VIP values exceeding 1.6 were selected as metabolite cut-off. Four compounds from the VIP plot were tested by the FDR (false discovery rate) method. Three compounds (which have three highest VIP scores) were found with the lowest FDR value of 6.7% (q = 0.067): PC (42:4p), PC (42:8), TG (18:1/18:2/18:2). Further, Receiver Operating Characteristic (ROC) curve analysis was used to evaluate the performance of the selected compounds. The higher values (close to 1) of AUC, the better confidence of biomarker compounds. We found PC (42:4p)H, and PC (42:8)H with AUC of 1.0, and TG (18:1/18:2/18:2) with AUC of 0.944, validating the importance of these three compounds. Between-group comparisons of these compounds are shown in Fig. 2h–j (red is PE/PSS, green is control).

2.5. Analysis of lipid classes and validation of Raman with LC-MS

Analysis of alterations to lipid classes was performed by summing all species within a class within each animal and comparing the group means of between PE/PSS and control with a *t*-test. Overall, phospholipid species consisted of 15/33 total measured lipid species and tended to be downregulated. In total, eight lipid species showed significant differences between groups. Only two lipid species were significantly upregulated, ChE and TG, and six downregulated, including the phospholipids PC, PA, PG, and dMePE, in addition to CL and GM1 (Fig. 2c). The corresponding Raman map for control and PE/PSS showing the distribution of cholesterol palmitate in the HPC are presented in Fig. 2d and e respectively. The corresponding quantification of cholesterol palmitate averaged from the Raman maps of each animal in the dHC region are shown in Fig. 2f and g. The results in Fig. 2f show that there is a significant increase of cholesterol palmitate in the dHC region of the brain in the PE/PSS group compared to the control group. LC-MS exhibited a significant 45% increase of ChE species (t = 3.034, df = 10, p = .0126). Results shown in Fig. 2g therefore, validate the Raman map results. The Raman map in Fig. 3a and b and the corresponding Raman image analysis (Fig. 3c), as well as LC-MS results (Fig. 3d) of TG, showed similar changes to cholesterol with an increased level in PE/PSS compared to the control group. The LC-MS data exhibited a significant 24% increase of TG species (t = 2.843, df = 10, p = .0175). However, Phosphatidylcholine (PC) (Fig. 3e–h) and Phosphatidylserine (PS) (Fig. 3i-l) were reduced in the dHPC region of the PE/PSS group compared to the control group. We observed a significant 44% decrease in PC species (t = 2.476, df = 10, p = .0328), but only a trend toward the reduction in PS (t = 2.077, df = 10, p = .0645) measured by LC-MS, providing validation for PC and near validation for PS. We also observed a significant 53% decrease in CL species (t = 2.4, df = 10, p = .0373), the opposite of the Raman results, and no significant difference in PI (t = 1.171, df = 10, p = .2686), all analyzed by a two-tailed unpaired *t*-test (Supplementary Figs. 1a–h). Overall, we were able to validate ChE, PC, PS, and TG, endpoints chosen from past data and Raman (ChE), and the VIP plot, but not CL and PI, targets not chosen from existing data. All of the above Raman images were constructed using the DCLS method.

We observed trends in the LC-MS data towards a reduction in total lipid species, not including CHOL, ChE, or TG (p = .069) (Fig. 4a) and total phospholipids (p = .06) (Supplementary Fig. 1k). We also observed a significant reduction when considering only the downregulated lipid species (t = 2.266, df = 10, p = .047) (Fig. 4b). These data support the Raman data exhibiting increased CHOL, which was not quantified in LC-MS, although we did measure and validate increased ChE. The LC-MS data was normalized by sample mass, therefore, we should expect to

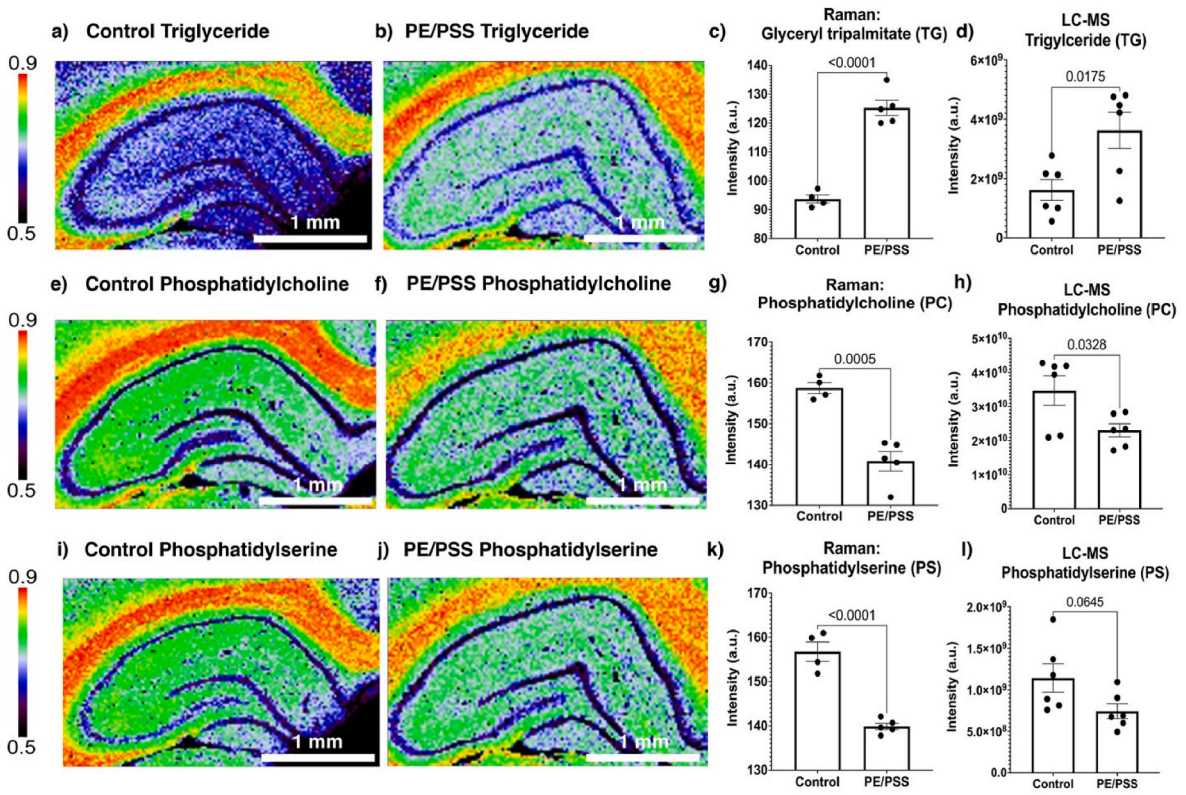

Fig. 3. Raman imaging comparison to LC-MS data for triglyceride (TG), phosphatidylcholine (PC), and phosphatidylserine (PS). a,b) Raman heatmap for TG for control and PE/PSS. c) quantification of Raman heatmap for TG. d) LC-MS data for TG. e, f) Raman heatmap for PC for control and PE/PSS. g) Quantification of Raman heatmap for PC. h) LC-MS data for PC. i, j) Raman heatmap for PS for control and PE/PSS. k) Quantification of Raman heatmap for PS. l) LC-MS data for PS. In all of the Raman maps, the colorbar represents the correlation coefficient and the scalebar = 1 mm.

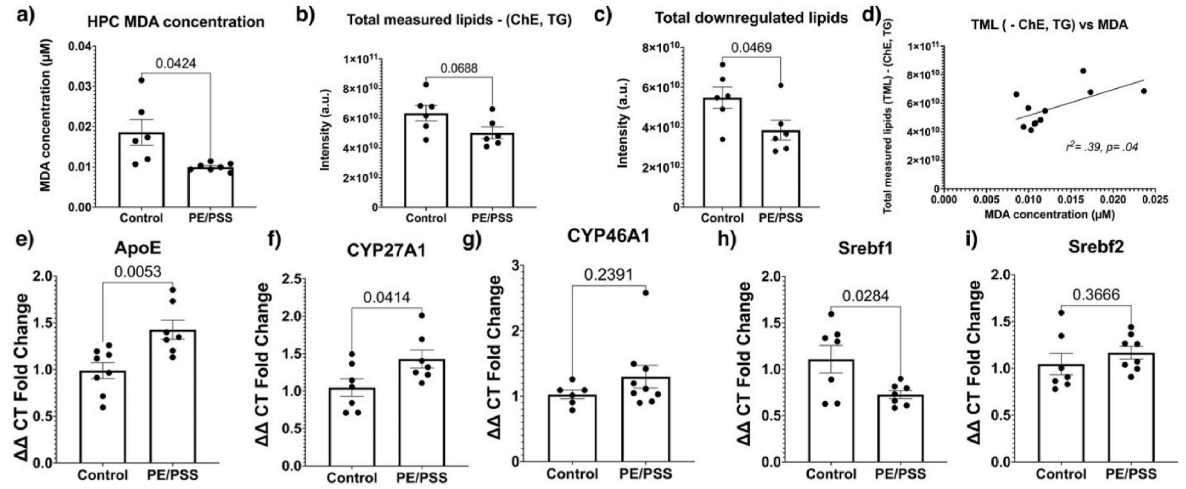

Fig. 4. a) Malondialdehyde (MDA) concentration in whole HPC tissue is reduced in PE/PSS vs control. b) Sum of total measured lipids not including cholesterol esters (ChE) or triglycerides (TG) between groups measured by LC-MS. c) Sum of all downregulated lipid species between groups exhibits significant reduction in these lipid species in PE/PSS d) Linear regression analysis of TML - (ChE, TG) vs MDA concentrations exhibits significant positive relationship between MDA and TML. e-i) PCR measure of relative mRNA abundance between control and PE/PSS. e) PCR measure of ApoE mRNA expression exhibits significantly greater ApoE in PE/PSS vs control. f) PCR measure of CYP27A1 mRNA expression exhibits significantly greater CYP27A1 expression in PE/PSS vs control. g) PCR measure of CYP46A1 expression does not exhibit significant differences between groups. h) PCR measure of Srebf1 exhibits significantly lower expression in PE/PSS vs control. i) PCR measure of Srebf2 exhibits no difference in expression between PE/PSS and control.

observe a proportional downregulation of other lipid species in LC-MS to the observed upregulation in CHOL in Raman. This provides additional validation of our Raman results for CHOL.

2.6. PE/PSS is associated with reduced MDA concentrations in the HPC, significant correlation with reduced measured lipids (not including CHOL, ChE, or TG)

Malondialdehyde (MDA) concentrations were measured using an

MDA assay. Variance differed between groups ($f = 65.76, 5, 6, p < .0001$), and therefore Welch's *t*-test was used for the analysis. MDA concentrations were reduced in PE/PSS compared to control ($t = 2.686$, $df = 5.13$, $p = .0424$) (Fig. 4c). Reduced MDA concentrations were significantly negatively correlated with total measured lipids (TML) (Not including CHOL, ChE, or TG) ($n = 11$, $R^2 = 0.3725$, $p = .0461$) (Fig. 4d), suggesting that reduced total lipids may partially mediate reduced MDA concentrations despite, or in response to, elevated ROS production.

2.7. PE/PSS is associated with increased ApoE and Cyp27a1 expression, and reduced expression of SREBF1

We performed qRT-PCR to examine differential expression of the following genes within the whole HPC of PE/PSS versus control rats: Abca1, Hmgcr, ApoE, Cyp46a1, Srebf2, Srebf1, Cyp27a1, Lrp1, Lxrb, and Ldlr. Of these main transcriptional drivers of CNS cholesterol and lipid maintenance, only ApoE ($t = 3.339$, $df = 13$, $p = .0053$), Srebf1 ($t = 2.490$, $df = 12$, $p = .0284$), and Cyp27a1 ($t = 2.283$, $df = 12$, $p = .0414$) showed significant differences in mRNA expression between PE/PSS and control groups using an unpaired *t*-test (Fig. 4e–i). There was a marked 44% increase in the expression of ApoE, the gene responsible for the transfer of cholesterol between cells, in the PE/PSS group versus control. CYP27a1 also exhibited an approximate 37% increase in expression in the HPC of the PE/PSS group versus control. However, there was a 53% decrease in the expression of Srebf1 compared to the control. All other genes assessed did not show statistically significant differences (Supplemental Fig. 1i-o).

3. Discussion

This study and emerging evidence from other labs suggests that lipid and CHOL homeostasis are altered by stress and glucocorticoids (GCC) and play a role in stress-induced disease states (Clement et al., 2009). The E4 polymorphism at the ApoE gene, which codes for a CHOL transporter, may be related to PTSD symptom severity, particularly intrusion and re-experiencing symptoms (Mota et al., 2018), which likely involve the HPC pattern separation function and fear generalization (Leal and Yassa, 2018). APOE4 also confers an increased risk of late-onset Alzheimer's disease and is associated with memory impairments (Bertram et al., 2007). In line with this, numerous lipid species including CHOL (Cartocci et al., 2017), ceramides, sphingolipids (Schneider et al., 2017), PC (Whiley et al., 2014), PI (Ulmann et al., 2001), and PS (Glade and Smith, 2015) are implicated in neural function and alterations to lipid homeostasis are associated with cognitive and memory impairment and neurodegenerative disease.

Chronic stress leads to HPC memory processing deficits and chronically elevated glucocorticoids (GCC)/elevated HPA axis/GCC sensitivity, reactive oxygen and nitrogen species (ROS/RNS), and inflammation, all of which have been observed in this model (Wilson et al., 2013, 2014a; Kelley et al., 2022). Excess GCC, ROS, or inflammation can lead to reduced neurogenesis and neuroplasticity (Mattson et al., 2008) and a greater propensity for excitotoxicity *in vitro* (Fogal and Hewett, 2008). Short-term glutamatergic excitotoxicity reduces cholesterol (CHOL) concentrations (Sodero et al., 2012), but chronic excitotoxicity increases it (Ong et al., 2010). ROS/oxidative stress, inflammation, and glucocorticoids may therefore mediate stress-induced functional alterations in the HPC and MTL through modulations to cholesterol and lipid homeostasis.

CHOL cannot cross blood brain barrier, therefore all CNS CHOL is synthesized locally from acetyl-CoA into 3-hydroxyl-3-methylglutaryl-coenzyme A (HMG-CoA) through HMG-CoA-synthetase and HMG-CoA reductase (Orth and Bellosta, 2012). The standard model is that CHOL is synthesized in astrocytes and transported to neurons by apolipoproteins like ApoE (Dietschy, 2009), but recent evidence also suggests that CHOL can be synthesized in neurons through distinct pathways (Genaro-Mattos et al., 2019). Likewise, most circulating ApoE is synthesized in the liver, but ApoE found in the CNS is synthesized locally (Boyles et al., 1985).

CHOL homeostasis is a major regulator of cell and organelle membrane fluidity and therefore modulates membrane receptor organization and the propensity for receptor dimerization and oligomerization, with important implications for cell signaling and neurotransmission (Prasanna et al., 2016, 2020). One of the primary receptors studied in this respect is the serotonin 5-HT_{1A}R, which contains a CHOL recognition/interaction amino acid consensus (CRAC) motif (Sengupta and Chattopadhyay, 2012a). This receptor plays a major role in brain development and psychiatric disease, including depression, PTSD, and general anxiety disorder (GAD), for which the major FDA-approved therapeutics, tricyclic antidepressants (TCA), and selective serotonin reuptake inhibitors (SSRIs) acutely increase serotonin (5-HT) levels. We have previously shown that 5-HT levels are reduced in the PFC and HPC of this PE/PSS model and are subsequently increased by Sertraline (SSRI) treatment (Wilson et al., 2014b). SSRIs block SERT (Slc6a4), the 5-HT transporter, acutely increasing extracellular 5-HT levels, but in humans, their AD effects require up to two weeks to take effect (Chu and Wadhwa, 2021). The canonical view is that their antidepressant (AD) effects are mediated by increased activation of cortical 5-HT_{1A}R and delayed neurochemical adaptations, like the desensitization of the 5-HT_{1A}R autoreceptor in the Raphe Nucleus to acutely increased 5-HT levels (Stahl, 1998). However, more recent work suggests a critical role of BDNF-TrkB signaling downstream of 5-HT signaling (Rantamäki, 2019; Casarotto et al., 2021a; Castrén and Monteggia, 2021). 5-HT_{1A}R is a G protein-coupled receptor that undergoes clathrin-mediated endocytosis upon stimulation and traffics along the endosomal recycling pathway. Upon Statin-induced CHOL depletion, the endocytic pathway shifts towards caveolin mediated endocytosis and a greater number of 5-HT_{1A}R are rerouted towards lysosomal degradation (Kumar and Chattopadhyay, 2020). 5-HT_{1A}R also exhibits increased CHOL-dependent conformational plasticity, increasing its propensity to dimerize with other 5-HT_{1A}Rs and potentially with other receptor types (Prasanna et al., 2016) with important effects on serotonergic neurotransmission. Furthermore, other 5-HT receptor subtypes, like the 5-HT_{2A}R, also dimerize to other GPCRs, and this process may likewise be mediated by CHOL concentrations in the cell membrane (Borroto-Escuela et al., 2021).

AD effects may also be dependent on TrkB activation downstream of serotonin receptors or glutamatergic NMDAR (Castrén and Monteggia, 2021). However, in contrast to this view, recent work has exhibited that TCA and SSRI AD and the recently FDA approved fast-acting AD Ketamine bind directly to TrkB receptors (Casarotto et al., 2021a), receptor tyrosine kinases that mediate brain-derived neurotropic factor (BDNF) signaling, which is a critical mediator of activity-dependent neuronal plasticity (Castrén and Antila, 2017) and the effects of all known AD drugs (Castrén and Monteggia, 2021). Casarotto and colleagues exhibited that mutation of the TrkB AD-binding motif impaired behavioral, cellular, and plasticity-promoting effects of AD *in vivo* and *in vitro*. (Casarotto et al., 2021a). BDNF signaling increases membrane CHOL concentrations (Suzuki et al., 2007), and CHOL concentrations tune TrkB signaling. The TrkB transmembrane domain (TMD) senses changes in membrane CHOL levels through a CRAC domain. Casarotto and colleagues depleted CHOL and observed reduced TrkB signaling; however, further increases in membrane CHOL concentrations beyond control levels also reduced TrkB signaling, exhibiting the bi-directional effects of CHOL levels on BDNF signaling. These effects were additionally rescued by AD treatment, exhibiting the complex relationships between CHOL, BDNF-TrkB signaling and AD treatment.

Here, we observed increased ROS production, increased CHOL, ChE, and TG, reduced phospholipids, including PC, PS, and PG, and reduced MDA concentrations, a marker of oxidative stress stemming from oxidized polyunsaturated fatty acids (Draper et al., 1993). MDA concentrations were correlated with reduced total lipid species (not

including CHOL, ChE, and TG). Using Raman, we also observed an increased peak at 1660 cm^{-1} in PE/PSS vs. control, which indicates the increased presence of DHA, a highly protective lipid species against oxidative stress (Wu et al., 2011). The shift observed here towards relatively increased CHOL/ChE and TG and lower levels of other lipids, predominantly phospholipids, which correlate with reduced MDA concentrations, may indicate a homeostatic response by cells in the HPC to reduce their propensity for OXS. It was unexpected to observe reduced MDA in this model despite increased ROS production, but this fact exemplifies the adaptive capacity of organisms to function across a broad range of homeostatic setpoints. This point is further supported by increased DHA concentrations in PE/PSS animals, suggesting a shift towards lipid species that are resistant to oxidative stress (OXS).

Finally, we investigated possible molecular mechanisms underpinning alterations to lipid homeostasis in this model. We sought to provide initial data in this area by performing qRT-PCR for ten important mediators of lipid synthesis, transport, or metabolism. We hypothesized that ApoE, Cyp27a1, and Srebf2 would be upregulated in PE/PSS and that Srebf1 would be down-regulated. We observed upregulated CHOL and therefore we expected increased CHOL synthesis (Srebf2), transport (ApoE), and metabolism (Cyp27a1). We rejected the null hypothesis for ApoE and Cyp27a1, but not Srebf2 (Fig. 4.). We also investigated six other transcripts associated with CHOL signaling or transport, but did not observe significant differences in any of those genes (Supplemental Fig. 1i-o).

ApoE is unable to cross the BBB (Liu et al., 2012) and is primarily generated by astrocytes in the CNS. ApoE is a major regulator of intracellular lipid homeostasis (Mauch et al., 2001) and exhibited increased expression in the PE/PSS group compared to the control. Increased ApoE expression is required for the transfer of cholesterol between CNS cell types to meet cellular demands for repair in the presence of cellular stress (Mahley and Huang, 2012). ROS and OXS is have a substantial impact on cellular viability of all neural cell types, but oligodendrocytes, cells that form myelin-sheaths and contribute up to 80% of the brain's total cholesterol are particularly sensitive (Chao et al., 2015; Dietschy, 2009; Schiavone et al., 2013). Stress and glucocorticoids increase oligodendrogenesis in the HPC (Chetty et al., 2014) and whole brain myelin concentrations are increased in human PTSD (Jak et al., 2020; Chao et al., 2015). Therefore, increased myelination of the HPC may contribute to the observed increased cholesterol here. ApoE plays a significant role in CNS response to injury (Poirier, 1996) and stress (Dose et al., 2016). ApoE also participates in the regulation of hippocampal neurogenesis and synaptogenesis (Yang et al., 2011). It's unknown if the increased ApoE expression and CHOL concentrations observed here play a role in regulating neurogenesis, oligodendrogenesis, or allostatic responses to stress, but it likely impacts all three and future investigations should focus on the role of ApoE expression and CHOL concentrations on these factors.

Srebf1 mediates the synthesis of monounsaturated and polyunsaturated fatty acids (MUFAs/PUFAs) in astrocytes, which commonly shuttle fatty acids to neurons, and is particularly significant in neurite outgrowth and synaptic transmission. Srebf2 mediates cholesterol synthesis (Camargo et al., 2009). In this study, we observed decreased Srebf1 and no significant change in Srebf2. Lower expression of Srebf1 is consistent with our observed trend towards a decrease in overall lipids not including CHOL, ChE, and TG. The lack of the expected increase in Srebf2 expression may indicate that increases in CHOL synthesis occurred earlier in the stress protocol from predator exposure on day 1 and 11 and were not sustained by psychosocial stress alone. Alternatively, there could be celling effects in the upregulation of CHOL by stress that occurred earlier in the protocol and while CHOL is still elevated, upregulated CHOL synthesis has since normalized. Specific investigations of this time course would be required to confirm this idea.

We did not observe differences in lipid expression between subregions of the HPC in this study (Fig. 1 g-i), but we did observe upregulated TG expression in the dHPC, while TG was observed to be downregulated in the paraventricular thalamus (PVT) in our previous work (Chaichi et al., 2021), exhibiting regionally-specific alterations to lipid species in this model. Stress-induced alterations to lipid expression may alter GPCR and tyrosine kinase receptor function (Kumar and Chattopadhyay, 2020; Prasanna et al., 2016, 2020; Sengupta and Chattopadhyay, 2012b; Casarotto et al., 2021b) in regionally-specific ways, underlining the importance of Raman's ability to detect such changes in animal models of stress-associated psychiatric disease, a novel capacity unavailable in most other existing techniques. To optimize the value of such observations, our method can be paired with immunohistochemistry to measure regionally-specific alterations to lipid species and receptors including 5-HT_{1A}, 5-HT_{2A}, SERT, and TrkB, the actions of which may be modulated by alterations to the brain lipidome. Numerous preclinical studies show that lipid concentrations in the membrane modulate the action of antidepressants and their target receptors (Kumar and Chattopadhyay, 2020; Prasanna et al., 2016, 2020; Sengupta and Chattopadhyay, 2012b; Casarotto et al., 2021b), but no studies have yet investigated the regionally specific effects of stress on the brain lipidome in tandem with these receptor targets. Future investigations in this area may have substantial implications for the use of antidepressant drugs in treatment resistant psychiatric disorders, like PTSD and depression.

This study exhibits the efficacy of Raman to image numerous lipid species *in situ* with confirmation by the gold standard, LC-MS. However, two of our "control" targets that were not either hypothesis driven from previous work, or among the top 15 targets that emerged from the LC-MS data, PI and PC, did not match the Raman data directionally. CL exhibited significant differences in both measures, but differed directionally, while PI exhibited a significant increase when measured by Raman, but no change when measured by LC-MS (Supplemental Figs. 1a–h). This could result from the fact that the lipid standards used for Raman were not representative of all lipid species measured by LC-MS. Individual variation within lipid species was expected and divergent expression of individual species was observed in some cases, although in most cases there were few divergently expressed individual lipid species within a lipid class. This discrepancy between the techniques could also result from the fact that Raman was only performed on *in situ* dHPC slices, while LC-MS was performed on extracted lipids from whole HPC tissue, including the ventral HPC. It's possible that PI is indeed increased in the dHPC, but not the ventral or that CL was divergently expressed across the D-V axis of the HPC. The decision to use whole HPC tissue for LC-MS was made to increase tissue availability such that aliquots of the same tissue could be used across LC-MS, qRT-PCR, and MDA assays. Divergent results between techniques could also exemplify limitations associated with using Raman to measure CL or PI species specifically and/or further standardization required for such measurements in fixed brain tissue. Another major limitation of this study was that we did not perform behavioral analysis on these animals to measure endpoints related to HPC function, nor did we experimentally modulate CHOL or other lipid levels to determine their effects on behavior. Future investigations should pair lipid analysis techniques, like Raman with behavioral analysis of HPC function, like object pattern separation, and modulate HPC cholesterol levels with statin drugs with and without PE/PSS to determine the causal impact of stress-induced CHOL and lipid concentrations on HPC function. We also did not directly measure oxidized lipid species. An MDA assay is only an index of oxidized PUFAs and is subject to off target effects. Direct measurements can be performed by LC-MS and such measures will be required for a complete evaluation of stress induced changes to oxidative and lipid homeostasis in this model system. Finally, we did not measure protein expression of lipid-related gene transcripts, antioxidant gene or protein expression, or Pla2, a gene implicated in inflammation that modulates lipid expression. Future investigations should measure protein expression of these targets to confirm expression changes at the functional level and measuring antioxidant protein expression will be required for a full evaluation of oxidative stress in this model. Biologically, this study

exhibits alterations to primary peripheral drivers of allostatic load (CHOL, TG, ROS, lipid metabolic pathway gene expression, and oxidative stress (MDA) in the HPC after PE/PSS, a model of PTSD. We observed that despite increased ROS and the typical sequela that follow, increased CHOL and TG, we did not observe increased MDA, a marker of OXS. Further, we did observe increased expression of DHA, a highly neuroprotective PUFA against OXS. Together, these data exemplify potential lipid metabolism-mediated mechanisms of biological adaption to increased ROS, preventing the development of allostatic overload exemplified by markers of OXS like MDA.

4. Experimental section/methods

4.1. Ethics statement

This study was performed in strict accordance with the recommendations of the Institute for Laboratory Animal Research's 2011 Guide for the Care and Use of Laboratory Animals, under the auspices of an animal care and use protocol approved by the Louisiana State University Institutional Animal Care and Use Committee 18–075. All animal experiments were performed according to ARRIVE guidelines.

4.2. Animals

Sprague Dawley rats were ordered from Charles River and were between 125 and 150 days old upon arrival. Animals were pair-housed in standard plastic microisolator cages and had access to food and water ad libitum. The cages were maintained in ventilated racks (8 × 5), and each cage was assigned a rack location at random to ensure even distribution of rack location. The vivarium was on a 12 h light/dark cycle (0700–1900) room temperature was maintained at 20 ± 1 °C and humidity ranged from 23 to 42%.

Two independent cohorts of animals were used for these experiments. One cohort n = 10/group was split into two groups such that n = 2–3/group were used for Raman and n = 7/group were used for EPR, PCR, and LC-MS. A second independent cohort of rats were only used to confirm the Raman data (n = 2–3/group). Predator exposures were performed using two cats, one male and one female (age 10, Harlan Laboratories, Indianapolis, IN, and age 13, Tulane University, New Orleans, LA, respectively). Cats were housed in an open room maintained at the same light/dark cycle, temperature, and humidity as the rat room.

4.3. Predator exposure and psychosocial stress (PE/PSS) model

Animals were pseudo-randomly assigned into either control or PE/PSS groups based on baseline body weight. PE/PSS rats began the stress regiment the following day. PE/PSS induction was performed as previously described.[95,40] Briefly, rats were placed into plexiglass cylinders, which were rubbed with cat food, and placed into a large metal cage where they were exposed to a live cat on day 1 and 11 of a 30 day stress regiment (PE). Every day from day 1–30 also required daily psychosocial stress (PSS), which consisted of cage rotation such that each stressed animal is paired with every other stressed animal before getting paired with a familiar rat again. Rats only experienced the same cage mate up to 3x per experiment.

4.4. Electron Paramagnetic Resonance Spectroscopy (EPR)

We measured ROS production by Electron Paramagnetic Resonance Spectroscopy (EPR) as previously published by our lab. [40,95] A separate aliquot from the same tissue homogenate was used for EPR, qRT-PCR, and the MDA assay. Immediately upon sacrifice, an aliquot of tissue was hand homogenized on a plastic dish submerged in ice and then plunged into ice cold buffer containing deferoxamine methanesulfonate (DF, 25 μmol/l) and diethyldithiocarbamic acid (DETC, 2.5 μmol/l) and the spin probe 1-hydroxy-3-methoxycarbonyl-2,2,5,5-tetramethyl-pyrrolidine (CMH) (200 μM), which was contained within a 24-well plate submerged on ice. CMH binds broadly to ROS, which are produced in relative proportion to *in vivo* production at physiological pH and temperature. We incubated tissue samples in CMH-containing buffer at physiological pH at 37 °C for 30 min directly prior to EPR measurements to produce a controlled release of ROS that mimics endogenous ROS production. When removed from the incubator, the 24-well plate containing tissue + buffer was subsequently plunged directly back into ice to stop the reaction, and aliquots of incubated probe media were then taken in 50 μl disposable glass capillary tubes (Noxygen Science Transfer and Diagnostics) for determination of ROS production. EPR measurements were performed using an EMX ESR eScan BenchTop spectrometer and superhigh quality factor microwave cavity (Bruker Company Germany) under the following settings: center field g = 2.002, field sweep 9.000 G, microwave power 20 mW, modulation amplitude 1.90 G, conversion time 10.24 ms, time constant 81.92 ms, and receiver gain, 3.17×10^3. Time Scan mode was used for the detection of ROS with the average of EPR amplitude every 10 scans over 10 min. These experiments were performed at 37 °C under 20 mm Hg of oxygen partial pressure using the Gas-Controller NOX-E.4-GC (Noxygen Science Transfer and Diagnostics GmbH). EPR measurements were normalized by the total sample protein using a Pierce BCA Protein Assay Kit (catalog number: 23,225).

4.5. Raman spectroscopy

4.5.1. Sample preparation for Raman

Animals were sacrificed on day 31 of the protocol. Animals were transcardially perfused with phosphate buffered saline (PBS) perfusion buffer until the fluid ran clear, and subsequently with 250 ml of 4% paraformaldehyde (PFA). Brains were then removed and incubated with 15% sucrose in PFA for 24 h and then 30% sucrose in PFA until the brain sank to the bottom of the solution. Brains were then stored at 4C until they were sectioned on a cryostat at 50 μm, which were then stored in 12 well plates at 4C until Raman was performed.

4.5.2. Raman imaging

Raman spectra were obtained with a Renishaw inVia Reflex Raman Spectroscope. The laser excitation wavelength of 785 nm, acquisition time of 20 s, and laser power of 30 mW were used. For the Raman map, static mode with a center wavenumber of 1200 cm^{-1}, with acquisition time of 4 s was used. Streamline Mapping (Y_{bin} = 20) mode of the Renishaw WiRE 4.4 software were used for fast image acquisition. The pixel resolution of the Raman map were 29.5 μm × 29.5 μm. The spatial dimensions of Raman map were ~2 mm × 4 mm. The total number of spectra in each brain tissue slice were ~10,000. The preprocessing, and principal component analysis (PCA) of spectra were performed in Origin (2018) (OriginLab, Northampton, MA). For the preprocessing of the spectral data, background fluorescence removal, min-max normalization, smoothing using Savitzky-Golay method were done. For the Savitzky-Golay method, the number of points of window = 25, polynomial order = 2 were used. The Raman map used direct classical least squares analysis (DCLS) method to analyze and to generate the lipid distributions. The Raman images were analyzed further using ImageJ 1.8 software. For the quatification of Raman maps (see Fig. S2), multiple tissue sections were imaged. We used n = 5 for the PE/PSS group, and n = 4 for Control group. We imaged two consecutive slices for 2 controls and 2 PTSD animals and confirmed that consecutive slices gave similar data. In all of these cases, the average of the duplicate slices were used for statistical analysis. DCLS algorithm is implemented in the WiRE 4.4 software of the Renishaw instrument (Fig. S3).

4.6. LC-MS lipidomics

4.6.1. Sample preparation for LC-MS

Animals were sacrificed on day 31 of the protocol. Upon sacrifice, the whole brain was removed in under 60 s and placed directly onto a cold plastic plate buried in ice. The whole HPC was immediately dissected by hand, hand homogenized on ice, and aliquoted for EPR, LC-MS, and qRT-PCR. For LC-MS, small aliquots of each sample were immediately flash frozen in aluminum foil. For tissue extraction, samples were weighed, recorded, and sonicated on ice until homogenous. The sample was transferred to an O-ring sealed screwed vial and 1 ml of solvent (chloroform: methanol (2:1 v/v)) was added. The samples were then shipped overnight on dry ice from the LSU School of Veterinary Medicine to the University of Illinois Urbana Champaign for lipidomic analysis by Dr. Zhang (Zhang et al., 2018).

4.6.2. Lipidomics, MS and data analysis

Samples were first sonicated with a Model Q700 QSonica sonicator equipped with an Oasis 180 Chiller (4 °C; amplitude, 95; process, 5 min; pulse on 30 s; plus off 55 s), centrifuged at 14,800 r.p.m. for 10 min at 4 °C, then 50 μl of the extract supernatant was spiked with 2 μl, 50 μg ml^{-1} internal standard mixture (Cer 18:1/12:0; PC 12:0/12:0; PE 14:0/14:0; PG 14:0/14:0; PS 14:0/14:0, etc). The samples were then analyzed using the Thermo Q-Exactive MS system in the Metabolomics Laboratory of the Roy J. Carver Biotechnology Center, University of Illinois at Urbana-Champaign. Xcalibur 3.0.63 was used for data acquisition and analysis (Zhang et al., 2018). A Dionex Ultimate 3000 series HPLC system (Thermo) was used, and LC separation was performed on a Thermo Accucore C18 column (2.1 × 150 mm, 2.6 μm) with mobile phase A (60% acetonitrile: 40% H2O with 10 mM ammonium formate and 0.1% formic acid) and mobile phase B (90% isopropanol: 10% acetonitrile with 10 mM ammonium formate and 0.1% formic acid) and a flow rate of 0.4 ml min^{-1}. The linear gradient was as follows: 0 min, 70% A; 4 min, 55% A; 12 min, 35% A; 18 min, 15% A; 20–25 min, 0% A; 26–33 min, 70% A. The autosampler was set to 15 °C and the column was kept at 45 °C. The injection volume was 10 μl. Mass spectra were acquired under both positive (sheath gas flow rate, 50; auxiliary gas flow rate, 13; sweep gas flow rate, 3; spray voltage, 3.5 kV; capillary temperature, 263 °C; auxiliary gas heater temperature, 425 °C) and negative (sheath gas flow rate, 50; auxiliary gas flow rate, 13; sweep gas flow rate, 3; spray voltage, −2.5 kV; capillary temperature, 263 °C; auxiliary gas heater temperature, 425 °C) electrospray ionization. The full scan mass spectrum resolution was set to 70,000 with a scan range of m/z ~230–1600 and the automatic gain control (AGC) target was 1E6 with a maximum injection time of 200 ms. For MS/MS scans, the mass spectrum resolution was set to 17,500 and the AGC target was 5E4 with a maximum injection time of 50 ms. The loop count was 10. The isolation window was 1.0 m/z with normalized collision energy (NCE) of 25 and 30 eV. LipidSearch (v.4.1.30, Thermo) was used for data analysis and lipid identification. Lipid signal responses were normalized to the corresponding internal standard signal response. For those lipid classes without corresponding internal standard, positive lipid ion signals were normalized with the signal of internal standard Cer 18:1/12:0 and negative ion signals were normalized with the signal of internal standard PG 14:0/14:0. The percentage of lipid classes within a sample was calculated by adding that of each of the individual molecular species quantified within a specific lipid class, and the relative abundance was represented by the mean percentage of three replicates for each group of samples. Abundance data was subsequently normalized by the mass of the sample.

4.6.3. Relative quantification of gene expression by real-time PCR

Whole hippocampal tissue was placed in TRIzol reagent according to manufacturer's instruction (Life Technologies) and stored at −80 °C until RNA extraction. Total RNA was extracted using a Qiagen Lipid Tissue Mini Kit Cat. No. 74804, and aliquots per gene were prepared for real time RT-PCR confirmation of those data. RNA quality and quantity were measured by Nanodrop Spectrophotometer ND-1000 UV/Vis. Real-time RT-PCR (n = 7–8) was used to confirm the mRNA levels of differentially expressed genes explained by RNA sequencing in the hippocampus (Abc1, Hmgcr, Cyp46al, Cyp27a1, Srebf1, Srebf2, ApoE, LxrB, Lrp1, and Ldlr). All 10 genes were run on at least 3 replicates across 2 PCR runs, totaling 6 runs/gene/sample. Reverse transcription of RNA was performed by using primers generated by PrimerQuest Tool (Integrated DNA Technologies). Total RNA extraction was performed as aforementioned. cDNA synthesis was performed using a Bio-Rad iScript cDNA synthesis kit (Catalog # 1708891) as previously reported (Sriramula et al., 2008). Gene expression was calculated by ΔΔCT and was normalized to GAPDH mRNA levels. These data are presented as fold change of the gene of interest relative to control animals. Table of primers (Supplemental Table 1).

4.6.4. Malondialdehyde (MDA) assay

Tissue samples of the whole HPC were flash frozen immediately upon extraction and stored in aluminum foil at −80 °C. Upon removal, tissue samples were homogenated in RIPA buffer, aliquoted, and frozen at −80 °C until the assay was performed. A lipid peroxidation malondialdehyde (MDA) assay kit was purchased from Abcam (ab118970) and utilized for MDA measurements per the manufacturer's instructions.

Supporting Information is available.

Ethics approval

This study was performed in strict accordance with the recommendations of the Institute for Laboratory Animal Research's 2011 Guide for the Care and Use of Laboratory Animals, under the auspices of an animal care and use protocol approved by the Louisiana State University Institutional Animal Care and Use Committee 18–075. All animal experiments were performed according to ARRIVE guidelines.

CRediT authorship contribution statement

D. Parker Kelley: conceived of the project., carried out all animal experiments, performed EPR, and performed statistics on EPR data, extracted lipids for LC-MS with assistance from, and, wrote the methods, results, and discussion sections for Raman and assisted with the LC-MS sections. **Ardalan Chaichi:** Formal analysis, conceived of the project., performed RAMAN and analyzed those data, performed PCR with assistance from. **Alexander Duplooy:** wrote the methods, results, and discussion sections for PCR. **Dhirendra Singh:** performed the MDA assay and performed statistical analysis on the PCR and MDA data, wrote the majority of the manuscript including the methods, results, and discussion section for the animal model, EPR, the MDA assay, and a large portion of the LC-MS lipidomics sections, conceived of the project. **Manas Ranjan Gartia:** conceived of the project. wrote the methods, results, and discussion sections for Raman and assisted with the LC-MS sections. **Joseph Francis:** conceived of the project.

Declaration of competing interest

The authors have no other relevant financial or non-financial interests to disclose.

Data availability

Data will be made available on request.

Acknowledgements

We would like to thank the Louisiana State University School of Veterinary Medicine Laboratory animal staff for their support of this project. Their cooperation and hard work was crucial for our success. We

would also like to thank Dr. C. Brad Wilson for establishing the experimental model in our lab. We thank Dr. Li Zhong for the LC-MS experiments. Manas Ranjan Gartia was supported by National Science Foundation (NSF CAREER award number: 2045640).

Appendix A. Supplementary data

Supplementary data to this article can be found online at https://doi.org/10.1016/j.ynstr.2022.100476.

References

Barres, B.A., Smith, S.J., 2001. Cholesterol–making or breaking the synapse. Science 294 (5545), 1296–1297.

Barrett, L.F., Quigley, K.S., Hamilton, P., 2016. An active inference theory of allostasis and interoception in depression. Phil. Trans. Biol. Sci. 371 (1708), 20160011 https://doi.org/10.1098/rstb.2016.0011. Somvanshi, P. R.; Mellon, S. H.; Flory, J. D.; Abu-Amara, D.; Consortium, P. S. B.; Wolkowitz, O. M.; Yehuda, R.; Jett, M.; Hood, L.; Marmar, C. Mechanistic inferences on metabolic dysfunction in posttraumatic stress disorder from an integrated model and multiomic analysis: role of glucocorticoid receptor sensitivity. American Journal of Physiology-Endocrinology and Metabolism 2019, 317 (5), E879-E898. DOI: 10.1152/ajpendo.00065.2019.

Bertram, L., McQueen, M.B., Mullin, K., Blacker, D., Tanzi, R.E., 2007. Systematic meta-analyses of Alzheimer disease genetic association studies: the AlzGene database. Nat. Genet. 39 (1), 17–23. https://doi.org/10.1038/ng1934.

Borroto-Escuela, D.O., Ambrogini, P., Narvaez, M., Di Liberto, V., Beggiato, S., Ferraro, L., Fores-Pons, R., Alvarez-Contino, J.E., Lopez-Salas, A., Mudò, G., et al., 2021. Serotonin heteroreceptor complexes and their integration of signals in neurons and astroglia-relevance for mental diseases. Cells 10 (8). https://doi.org/10.3390/cells10081902. From NLM.

Boyles, J.K., Pitas, R.E., Wilson, E., Mahley, R.W., Taylor, J.M., 1985. Apolipoprotein E associated with astrocytic glia of the central nervous system and with nonmyelinating glia of the peripheral nervous system. J. Clin. Invest. 76 (4), 1501–1513. https://doi.org/10.1172/jci112130. From NLM.

Cajka, T., Fiehn, O., 2014. Comprehensive analysis of lipids in biological systems by liquid chromatography-mass spectrometry. Trends Anal. Chem. 61, 192–206. https://doi.org/10.1016/j.trac.2014.04.017. From NLM.

Camargo, N., Smit, A.B., Verheijen, M.H., 2009. SREBPs: SREBP function in glia-neuron interactions. FEBS J. 276 (3), 628–636. https://doi.org/10.1111/j.1742-4658.2008.06808.x. From NLM.

Cartocci, V., Servadio, M., Trezza, V., Pallottini, V., 2017. Can cholesterol metabolism modulation affect brain function and behavior? J. Cell. Physiol. 232 (2), 281–286.

Casarotto, P.C., Girych, M., Fred, S.M., Kovaleva, V., Moliner, R., Enkavi, G., Biojone, C., Cannarozzo, C., Sahu, M.P., Kaurinkoski, K., et al., 2021a. Antidepressant drugs act by directly binding to TRKB neurotrophin receptors. e1219 Cell 184 (5), 1299–1313. https://doi.org/10.1016/j.cell.2021.01.034. From NLM.

Casarotto, P.C., Girych, M., Fred, S.M., Kovaleva, V., Moliner, R., Enkavi, G., Biojone, C., Cannarozzo, C., Sahu, M.P., Kaurinkoski, K., et al., 2021b. Antidepressant drugs act by directly binding to TRKB neurotrophin receptors. e1219 Cell 184 (5), 1299–1313. https://doi.org/10.1016/j.cell.2021.01.034. From NLM.

Castrén, E., Antila, H., 2017. Neuronal plasticity and neurotrophic factors in drug responses. Mol. Psychiatr. 22 (8), 1085–1095. https://doi.org/10.1038/mp.2017.61. . Huang, Z. J.; Kirkwood, A.; Pizzorusso, T.; Porciatti, V.; Morales, B.; Bear, M. F.; Maffei, L.; Tonegawa, S. BDNF regulates the maturation of inhibition and the critical period of plasticity in mouse visual cortex. Cell 1999, 98 (6), 739-755. DOI: 10.1016/s0092-8674(00)81509-3 From NLM.

Castrén, E., Monteggia, L.M., 2021. Brain-derived neurotrophic factor signaling in depression and antidepressant action. Biol. Psychiatr. 90 (2), 128–136. https://doi.org/10.1016/j.biopsych.2021.05.008. From NLM.

Chaichi, A., Hasan, S.M.A., Mehta, N., Donnarumma, F., Ebenezer, P., Murray, K.K., Francis, J., Gartia, M.R., 2021. Label-free lipidome study of paraventricular thalamic nucleus (PVT) of rat brain with post-traumatic stress injury by Raman imaging. Analyst 146 (1), 170–183.

Chao, L.L., Tosun, D., Woodward, S.H., Kaufer, D., Neylan, T.C., 2015. Preliminary evidence of increased hippocampal myelin content in veterans with posttraumatic stress disorder. Front. Behav. Neurosci. 9, 333. https://doi.org/10.3389/fnbeh.2015.00333. From NLM.

Chetty, S., Friedman, A.R., Taravosh-Lahn, K., Kirby, E.D., Mirescu, C., Guo, F., Krupik, D., Nicholas, A., Geraghty, A., Krishnamurthy, A., et al., 2014. Stress and glucocorticoids promote oligodendrogenesis in the adult hippocampus. Mol. Psychiatr. 19 (12), 1275–1283. https://doi.org/10.1038/mp.2013.190. From NLM.

Chu, A., Wadhwa, R., 2021. Selective serotonin reuptake inhibitors. In: *StatPearls*, StatPearls Publishing Copyright © 2021. StatPearls Publishing LLC.

Chung, S.-Y., Moriyama, T., Uezu, E., Uezu, K., Hirata, R., Yohena, N., Masuda, Y., Kokubu, Y., Yamamoto, S., 1995. Administration of phosphatidylcholine increases brain acetylcholine concentration and improves memory in mice with dementia. J. Nutr. 125 (6), 1484–1489. Jope, R. S. Effects of phosphatidylcholine administration to rats on choline in blood and choline and acetylcholine in brain. Journal of Pharmacology and Experimental Therapeutics 1982, 220 (2), 322-328.

Clement, A.B., Gamerdinger, M., Tamboli, I.Y., Lütjohann, D., Walter, J., Greeve, I., Gimpl, G., Behl, C., 2009. Adaptation of neuronal cells to chronic oxidative stress is associated with altered cholesterol and sphingolipid homeostasis and lysosomal function. J. Neurochem. 111 (3), 669–682. https://doi.org/10.1111/j.1471-4159.2009.06360 x From NLM. Anchisi, L.; Dessì, S.; Pani, A.; Mandas, A. Cholesterol homeostasis: a key to prevent or slow down neurodegeneration. Front Physiol 2012, 3, 486. DOI: 10.3389/fphys.2012.00486 From NLM.

Cornelius, C., Crupi, R., Calabrese, V., Graziano, A., Milone, P., Pennisi, G., Radak, Z., Calabrese, E.J., Cuzzocrea, S., 2013. Traumatic brain injury: oxidative stress and neuroprotection. Antioxidants Redox Signal. 19 (8), 836–853. https://doi.org/10.1089/ars.2012.4981. From NLM.

Czamara, K., Majzner, K., Pacia, M.Z., Kochan, K., Kaczor, A., Baranska, M., 2015. Raman spectroscopy of lipids: a review. J. Raman Spectrosc. 46 (1), 4–20.

Demirkan, A., Isaacs, A., Ugocsai, P., Liebisch, G., Struchalin, M., Rudan, I., Wilson, J.F., Pramstaller, P.P., Gyllensten, U., Campbell, H., et al., 2013. Plasma phosphatidylcholine and sphingomyelin concentrations are associated with depression and anxiety symptoms in a Dutch family-based lipidomics study. J. Psychiatr. Res. 47 (3), 357–362. https://doi.org/10.1016/j.jpsychires.2012.11.001. From NLM.

Dietschy, J.M., 2009. Central nervous system: cholesterol turnover, brain development and neurodegeneration. Biol. Chem. 390 (4), 287–293. https://doi.org/10.1515/bc.2009.035. From NLM.

Dose, J., Huebbe, P., Nebel, A., Rimbach, G., 2016. APOE genotype and stress response - a mini review. Lipids Health Dis. 15, 121. https://doi.org/10.1186/s12944-016-0288-2. From NLM.

Draper, H.H., Squires, E.J., Mahmoodi, H., Wu, J., Agarwal, S., Hadley, M., 1993. A comparative evaluation of thiobarbituric acid methods for the determination of malondialdehyde in biological materials. Free Radic. Biol. Med. 15 (4), 353–363. https://doi.org/10.1016/0891-5849(93)90035-s. From NLM.

Fester, L., Zhou, L., Bütow, A., Huber, C., Von Lossow, R., Prange-Kiel, J., Jarry, H., Rune, G.M., 2009. Cholesterol-promoted synaptogenesis requires the conversion of cholesterol to estradiol in the hippocampus. Hippocampus 19 (8), 692–705.

Fogal, B., Hewett, S.J., 2008. Interleukin-1β: a bridge between inflammation and excitotoxicity? J. Neurochem. 106 (1), 1–23.

Furukawa, S., Fujita, T., Shimabukuro, M., Iwaki, M., Yamada, Y., Nakajima, Y., Nakayama, O., Makishima, M., Matsuda, M., Shimomura, I., 2004. Increased oxidative stress in obesity and its impact on metabolic syndrome. J. Clin. Invest. 114 (12), 1752–1761. https://doi.org/10.1172/jci21625. From NLM.

Genaro-Mattos, T.C., Anderson, A., Allen, L.B., Korade, Z., Mirnics, K., 2019. Cholesterol biosynthesis and uptake in developing neurons. ACS Chem. Neurosci. 10 (8), 3671–3681. https://doi.org/10.1021/acschemneuro.9b00248. From NLM. Mitsche, M. A.; McDonald, J. G.; Hobbs, H. H.; Cohen, J. C. Flux analysis of cholesterol biosynthesis in vivo reveals multiple tissue and cell-type specific pathways. Elife 2015, 4, e07999. DOI: 10.7554/eLife.07999 From NLM.

Glade, M.J., Smith, K., 2015. Phosphatidylserine and the human brain. Nutrition 31 (6), 781–786. https://doi.org/10.1016/j.nut.2014.10.014.

Goritz, C., Mauch, D.H., Pfrieger, F.W., 2005. Multiple mechanisms mediate cholesterol-induced synaptogenesis in a CNS neuron. Mol. Cell. Neurosci. 29 (2), 190–201. Tirtawijaya, G.; Haque, M. N.; Choi, J. S.; Moon, I. S.; Meinita, M. D. N.; Choi, J.-S.; Hong, Y.-K. Spinogenesis and synaptogenesis effects of the red seaweed Kappaphycus alvarezii and its isolated cholesterol on hippocampal neuron cultures. Preventive nutrition and food science 2019, 24 (4), 418.

Guidi, J., Lucente, M., Piolanti, A., Roncuzzi, R., Rafanelli, C., Sonino, N., 2020. Allostatic overload in patients with essential hypertension. Psychoneuroendocrinology 113, 104545. https://doi.org/10.1016/j.psyneuen.2019.104545. Sterling, P. Allostasis: a model of predictive regulation. Physiology & behavior 2012, 106 (1), 5-15. DOI: 10.1016/j.physbeh.2011.06.004. Mocayar Maron, F. J.; Ferder, L.; Saraví, F. D.; Manucha, W. Hypertension linked to allostatic load: from psychosocial stress to inflammation and mitochondrial dysfunction. Stress 2019, 22 (2), 169-181. DOI: 10.1080/10253890.2018.1542683.

Hu, C., Wang, M., Han, X., 2017. Shotgun lipidomics in substantiating lipid peroxidation in redox biology: methods and applications. Redox Biol. 12, 946–955. https://doi.org/10.1016/j.redox.2017.04.030.

Huguenard, C.J., Cseresznye, A., Evans, J.E., Oberlin, S., Langlois, H., Ferguson, S., Darcey, T., Nkiliza, A., Dretsch, M., Mullan, M., 2020. Plasma lipidomic analyses in cohorts with mTBI and/or PTSD reveal lipids differentially associated with diagnosis and APOE ε4 carrier status. Front. Physiol. 11, 12.

Jak, A.J., Jurick, S., Hoffman, S., Evangelista, N.D., Deford, N., Keller, A., Merritt, V.C., Sanderson-Cimino, M., Sorg, S., Delano-Wood, L., et al., 2020. PTSD, but not history of mTBI, is associated with altered myelin in combat-exposed Iraq and Afghanistan Veterans. Clin. Neuropsychol. 34 (6), 1070–1087. https://doi.org/10.1080/13854046.2020.1730975. From NLM. Langbroek, J.; Treur, J.; Ziabari, S. S. M. A computational model of myelin excess for patients with post-traumatic stress disorder. In International conference on artificial intelligence and soft computing, 2019; Springer: pp 203-215.

Kelley, D.P., Venable, K., Destouni, A., Billac, G., Ebenezer, P., Stadler, K., Nichols, C., Barker, S., Francis, J., 2022. Pharmahuasca and DMT rescue ROS production and differentially expressed genes observed after predator and psychosocial stress: relevance to human PTSD. ACS Chem. Neurosci. https://doi.org/10.1021/acschemneuro.1c00660. From NLM.

Korade, Z., Kenworthy, A.K., 2008. Lipid rafts, cholesterol, and the brain. Neuropharmacology 55 (8), 1265–1273.

Kumar, G.A., Chattopadhyay, A., 2020. Statin-induced chronic cholesterol depletion switches GPCR endocytosis and trafficking: insights from the serotonin(1A) receptor. ACS Chem. Neurosci. 11 (3), 453–465. https://doi.org/10.1021/acschemneuro.9b00659. From NLM.

Leal, S.L., Yassa, M.A., 2018. Integrating new findings and examining clinical applications of pattern separation. Nat. Neurosci. 21 (2), 163–173. https://doi.org/

10.1038/s41593-017-0065-1. From NLM. Lange, I.; Goossens, L.; Michielse, S.; Bakker, J.; Lissek, S.; Papalini, S.; Verhagen, S.; Leibold, N.; Marcelis, M.; Wichers, M. Behavioral pattern separation and its link to the neural mechanisms of fear generalization. Social cognitive and affective neuroscience 2017, 12 (11), 1720-1729. DOI: 10.1093/scan/nsx104.

Leslie, R.D., Vartak, T., 2020. Allostasis and the origins of adult-onset diabetes. Diabetologia 63 (2), 261–265. https://doi.org/10.1007/s00125-019-05048-9. Stumvoll, M.; Tataranni, P. A.; Stefan, N.; Vozarova, B.; Bogardus, C. Glucose allostasis. Diabetes 2003, 52 (4), 903-909. DOI: 10.2337/diabetes.52.4.903.

Lindqvist, D., Dhabhar, F.S., James, S.J., Hough, C.M., Jain, F.A., Bersani, F.S., Reus, V.I., Verhoeven, J.E., Epel, E.S., Mahan, L., et al., 2017. Oxidative stress, inflammation and treatment response in major depression. Psychoneuroendocrinology 76, 197–205. https://doi.org/10.1016/j.psyneuen.2016.11.031. From NLM.

Liu, M., Kuhel, D.G., Shen, L., Hui, D.Y., Woods, S.C., 2012. Apolipoprotein E does not cross the blood-cerebrospinal fluid barrier, as revealed by an improved technique for sampling CSF from mice. Am. J. Physiol. Regul. Integr. Comp. Physiol. 303 (9), R903–R908. https://doi.org/10.1152/ajpregu.00219.2012. From NLM.

Mahley, R.W., Huang, Y., 2012. Apolipoprotein e sets the stage: response to injury triggers neuropathology. Neuron 76 (5), 871–885. https://doi.org/10.1016/j.neuron.2012.11.020. From NLM.

Mateos, M.V., Uranga, R.M., Salvador, G.A., Giusto, N.M., 2008. Activation of phosphatidylcholine signalling during oxidative stress in synaptic endings. Neurochem. Int. 53 (6–8), 199–206.

Mattson, M.P., Gleichmann, M., Cheng, A., 2008. Mitochondria in neuroplasticity and neurological disorders. Neuron 60 (5), 748–766. https://doi.org/10.1016/j.neuron.2008.10.010.

Mauch, D.H., Nägler, K., Schumacher, S., Göritz, C., Müller, E.C., Otto, A., Pfrieger, F.W., 2001. CNS synaptogenesis promoted by glia-derived cholesterol. Science 294 (5545), 1354–1357. https://doi.org/10.1126/science.294.5545.1354. From NLM.

Miller, M.W., Lin, A.P., Wolf, E.J., Miller, D.R., 2018. Oxidative stress, inflammation, and neuroprogression in chronic PTSD. Harv. Rev. Psychiatr. 26 (2), 57–69. https://doi.org/10.1097/hrp.0000000000000167. From NLM.

Morell, P., Toews, A.D., 1996. Biochemistry of lipids. Handb. Clin. Neurol. 22 (66), 33–49.

Mota, N.P., Han, S., Harpaz-Rotem, I., Maruff, P., Krystal, J.H., Southwick, S.M., Gelernter, J., Pietrzak, R.H., 2018. Apolipoprotein E gene polymorphism, trauma burden, and posttraumatic stress symptoms in US military veterans: results from the National Health and Resilience in Veterans Study. Depress. Anxiety 35 (2), 168–177.

Movasaghi, Z., Rehman, S., Rehman, I.U., 2007. Raman spectroscopy of biological tissues. Appl. Spectrosc. Rev. 42 (5), 493–541.

Nuttall, S., Heaton, S., Piper, M., Martin, U., Gordon, C., 2003. Cardiovascular risk in systemic lupus erythematosus—evidence of increased oxidative stress and dyslipidaemia. Rheumatology 42 (6), 758–762.

Oliveira, T.G., Chan, R.B., Bravo, F.V., Miranda, A., Silva, R.R., Zhou, B., Marques, F., Pinto, V., Cerqueira, J.J., Di Paolo, G., 2016. The impact of chronic stress on the rat brain lipidome. Mol. Psychiatr. 21 (1), 80–88. https://doi.org/10.1038/mp.2015.14.

Ong, W.-Y., Kim, J.-H., He, X., Chen, P., Farooqui, A.A., Jenner, A.M., 2010. Changes in brain cholesterol metabolome after excitotoxicity. Mol. Neurobiol. 41 (2), 299–313. https://doi.org/10.1007/s12035-010-8099-3.

Orth, M., Bellosta, S., 2012. Cholesterol: its regulation and role in central nervous system disorders. Cholesterol 2012, 292598. https://doi.org/10.1155/2012/292598. From NLM. Petrov, A. M.; Kasimov, M. R.; Zefirov, A. L. Brain Cholesterol Metabolism and Its Defects: Linkage to Neurodegenerative Diseases and Synaptic Dysfunction. Acta Naturae 2016, 8 (1), 58-73. From NLM.

Payandeh, J., Volgraf, M., 2021. Ligand binding at the protein–lipid interface: strategic considerations for drug design. Nat. Rev. Drug Discov. 1–13.

Poirier, J., 1996. Apolipoprotein E in the brain and its role in Alzheimer's disease. J. Psychiatry Neurosci. 21 (2), 128–134. From NLM.

Prasad, A., Chaichi, A., Kelley, D.P., Francis, J., Gartia, M.R., 2019. Current and future functional imaging techniques for post-traumatic stress disorder. RSC Adv. 9 (42), 24568–24594. https://doi.org/10.1039/C9RA03562A.

Prasanna, X., Sengupta, D., Chattopadhyay, A., 2016. Cholesterol-dependent conformational plasticity in GPCR dimers. Sci. Rep. 6, 31858 https://doi.org/10.1038/srep31858. From NLM.

Prasanna, X., Mohole, M., Chattopadhyay, A., Sengupta, D., 2020. Role of cholesterol-mediated effects in GPCR heterodimers. Chem. Phys. Lipids 227, 104852. https://doi.org/10.1016/j.chemphyslip.2019.104852. From NLM.

Rantamäki, T., 2019. TrkB neurotrophin receptor at the core of antidepressant effects, but how? Cell Tissue Res. 377 (1), 115–124. https://doi.org/10.1007/s00441-018-02985-6. From NLM.

Reddy, D.S., 2010. Neurosteroids: endogenous role in the human brain and therapeutic potentials. Prog. Brain Res. 186, 113–137.

Santos, I.P., Caspers, P.J., Bakker Schut, T.C., van Doorn, R., Noordhoek Hegt, V., Koljenović, S., Puppels, G.J., 2016. Raman spectroscopic characterization of melanoma and benign melanocytic lesions suspected of melanoma using high-wavenumber Raman spectroscopy. Anal. Chem. 88 (15), 7683–7688. https://doi.org/10.1021/acs.analchem.6b01592. From NLM. Köhler, M.; Machill, S.; Salzer, R.; Krafft, C. Characterization of lipid extracts from brain tissue and tumors using Raman spectroscopy and mass spectrometry. Anal Bioanal Chem 2009, 393 (5), 1513-1520. DOI: 10.1007/s00216-008-2592-9 From NLM.

Schiavone, S., Jaquet, V., Trabace, L., Krause, K.H., 2013. Severe life stress and oxidative stress in the brain: from animal models to human pathology. Antioxidants Redox Signal. 18 (12), 1475–1490. https://doi.org/10.1089/ars.2012.4720. From NLM. Salim, S. Oxidative Stress and the Central Nervous System. J Pharmacol Exp Ther 2017, 360 (1), 201-205. DOI: 10.1124/jpet.116.237503 From NLM. Dietschy, J. M.; Turley, S. D. Thematic review series: brain Lipids. Cholesterol metabolism in the central nervous system during early development and in the mature animal. J Lipid Res 2004, 45 (8), 1375-1397. DOI: 10.1194/jlr.R400004-JLR200 From NLM.

Schneider, M., Levant, B., Reichel, M., Gulbins, E., Kornhuber, J., Müller, C.P., 2017. Lipids in psychiatric disorders and preventive medicine. Neurosci. Biobehav. Rev. 76 (Pt B), 336–362. https://doi.org/10.1016/j.neubiorev.2016.06.002.

Schultz, Z.D., Levin, I.W., 2011. Vibrational spectroscopy of biomembranes. Annu. Rev. Anal. Chem. 4, 343–366. https://doi.org/10.1146/annurev-anchem-061010-114048. From NLM. Schultz, Z. D. Raman Spectroscopic Imaging of Cholesterol and Docosahexaenoic Acid Distribution in the Retinal Rod Outer Segment. Aust J Chem 2011, 64 (5), 611-616. DOI: 10.1071/ch11019 From NLM. Wang, P.; Li, J.; Wang, P.; Hu, C. R.; Zhang, D.; Sturek, M.; Cheng, J. X. Label-free quantitative imaging of cholesterol in intact tissues by hyperspectral stimulated Raman scattering microscopy. Angew Chem Int Ed Engl 2013, 52 (49), 13042-13046. DOI: 10.1002/anie.201306234 From NLM.

Sengupta, D., Chattopadhyay, A., 2012a. Identification of cholesterol binding sites in the serotonin1A receptor. J. Phys. Chem. B 116 (43), 12991–12996. https://doi.org/10.1021/jp309888u. From NLM.

Sengupta, D., Chattopadhyay, A., 2012b. Identification of cholesterol binding sites in the serotonin1A receptor. J. Phys. Chem. B 116 (43), 12991–12996. https://doi.org/10.1021/jp309888u. From NLM.

Shan, L., Zhang, T., Fan, K., Cai, W., Liu, H., 2021. Astrocyte-Neuron signaling in synaptogenesis. Front. Cell Dev. Biol. 9, 1786.

Sodero, A.O., Vriens, J., Ghosh, D., Stegner, D., Brachet, A., Pallotto, M., Sassoè-Pognetto, M., Brouwers, J.F., Helms, J.B., Nieswandt, B., 2012. Cholesterol loss during glutamate-mediated excitotoxicity. EMBO J. 31 (7), 1764–1773. https://doi.org/10.1038/emboj.2012.31.

Stahl, S.M., 1998. Mechanism of action of serotonin selective reuptake inhibitors: serotonin receptors and pathways mediate therapeutic effects and side effects. J. Affect. Disord. 51 (3), 215–235. Gray, N. A.; Milak, M. S.; DeLorenzo, C.; Ogden, R. T.; Huang, Y. Y.; Mann, J. J.; Parsey, R. V. Antidepressant treatment reduces serotonin-1A autoreceptor binding in major depressive disorder. Biol Psychiatry 2013, 74 (1), 26-31. DOI: 10.1016/j.biopsych.2012.11.012 From NLM.

Surmacki, J.M., Ansel-Bollepalli, L., Pischiutta, F., Zanier, E.R., Ercole, A., Bohndiek, S. E., 2017. Label-free monitoring of tissue biochemistry following traumatic brain injury using Raman spectroscopy. Analyst 142 (1), 132–139.

Suzuki, S., Kiyosue, K., Hazama, S., Ogura, A., Kashihara, M., Hara, T., Koshimizu, H., Kojima, M., 2007. Brain-derived neurotrophic factor regulates cholesterol metabolism for synapse development. J. Neurosci. 27 (24), 6417–6427. https://doi.org/10.1523/JNEUROSCI.0690-07.2007. Zonta, B.; Minichiello, L. Synaptic membrane rafts: traffic lights for local neurotrophin signaling? Frontiers in synaptic neuroscience 2013, 5, 9.

Ulmann, L., Mimouni, V., Roux, S., Porsolt, R., Poisson, J.-P., 2001. Brain and hippocampus fatty acid composition in phospholipid classes of aged-relative cognitive deficit rats. Prostaglandins Leukot. Essent. Fatty Acids 64 (3), 189–195. https://doi.org/10.1054/plef.2001.0260.

Wertlake, P.T., Wilcox, A.A., Haley, M.I., Peterson, J.E., 1958. Relationship of mental and emotional stress to serum cholesterol levels. Proc. Soc. Exp. Biol. Med. 97 (1), 163–165. https://doi.org/10.3181/00379727-97-23676. From NLM.

Whiley, L., Sen, A., Heaton, J., Proitsi, P., García-Gómez, D., Leung, R., Smith, N., Thambisetty, M., Kloszewska, I., Mecocci, P., 2014. Evidence of altered phosphatidylcholine metabolism in Alzheimer's disease. Neurobiol. Aging 35 (2), 271–278. https://doi.org/10.1016/j.neurobiolaging.2013.08.001.

Wilson, C.B., McLaughlin, L.D., Nair, A., Ebenezer, P.J., Dange, R., Francis, J., 2013. Inflammation and oxidative stress are elevated in the brain, blood, and adrenal glands during the progression of post-traumatic stress disorder in a predator exposure animal model. PLoS One 8 (10), e76146. https://doi.org/10.1371/journal.pone.0076146. From NLM.

Wilson, C.B., Ebenezer, P.J., McLaughlin, L.D., Francis, J., 2014a. Predator exposure/psychosocial stress animal model of post-traumatic stress disorder modulates neurotransmitters in the rat hippocampus and prefrontal cortex. PLoS One 9 (2), e89104. https://doi.org/10.1371/journal.pone.0089104. From NLM. Zoladz, P. R.; Conrad, C. D.; Fleshner, M.; Diamond, D. M. Acute episodes of predator exposure in conjunction with chronic social instability as an animal model of post-traumatic stress disorder. Stress 2008, 11 (4), 259-281. DOI: 10.1080/10253890701768613 From NLM. Zoladz, P. R.; Fleshner, M.; Diamond, D. M. Psychosocial animal model of PTSD produces a long-lasting traumatic memory, an increase in general anxiety and PTSD-like glucocorticoid abnormalities. Psychoneuroendocrinology 2012, 37 (9), 1531-1545. DOI: 10.1016/j.psyneuen.2012.02.007. Zoladz, P. R.; Park, C. R.; Fleshner, M.; Diamond, D. M. Psychosocial predator-based animal model of PTSD produces physiological and behavioral sequelae and a traumatic memory four months following stress onset. Physiol Behav 2015, 147, 183-192. DOI: 10.1016/j.physbeh.2015.04.032 From NLM. Burke, H. M.; Robinson, C. M.; Wentz, B.; McKay, J.; Dexter, K. W.; Pisansky, J. M.; Talbot, J. N.; Zoladz, P. R. Sex-specific impairment of spatial memory in rats following a reminder of predator stress. Stress 2013, 16 (4), 469-476. DOI: 10.3109/10253890.2013.791276 From NLM. Woodson, J. C.; Macintosh, D.; Fleshner, M.; Diamond, D. M. Emotion-induced amnesia in rats: working memory-specific impairment, corticosterone-memory correlation, and fear versus arousal effects on memory. Learning & memory 2003, 10 (5), 326-336. DOI: 10.1101/lm.62903.

Wilson, C.B., McLaughlin, L.D., Ebenezer, P.J., Nair, A.R., Dange, R., Harre, J.G., Shaak, T.L., Diamond, D.M., Francis, J., 2014b. Differential effects of sertraline in a predator exposure animal model of post-traumatic stress disorder. Front. Behav. Neurosci. 8, 256. https://doi.org/10.3389/fnbeh.2014.00256. From NLM.

Wu, A., Ying, Z., Gomez-Pinilla, F., 2011. The salutary effects of DHA dietary supplementation on cognition, neuroplasticity, and membrane homeostasis after

brain trauma. J. Neurotrauma 28 (10), 2113–2122. https://doi.org/10.1089/neu.2011.1872. From NLM.

Yang, C.P., Gilley, J.A., Zhang, G., Kernie, S.G., 2011. ApoE is required for maintenance of the dentate gyrus neural progenitor pool. Development 138 (20), 4351–4362. https://doi.org/10.1242/dev.065540. From NLM. Tensaouti, Y.; Stephanz, E. P.; Yu, T. S.; Kernie, S. G. ApoE Regulates the Development of Adult Newborn Hippocampal Neurons. eNeuro 2018, 5 (4). DOI: 10.1523/eneuro.0155-18.2018 From NLM.

Zhang, H., Freitas, D., Kim, H.S., Fabijanic, K., Li, Z., Chen, H., Mark, M.T., Molina, H., Martin, A.B., Bojmar, L., et al., 2018. Identification of distinct nanoparticles and subsets of extracellular vesicles by asymmetric flow field-flow fractionation. Nat. Cell Biol. 20 (3), 332–343. https://doi.org/10.1038/s41556-018-0040-4. From NLM.